# ARTICLE     OPEN

Check for updates

# Anomalous hall and skyrmion topological hall resistivity in magnetic heterostructures for the neuromorphic computing applications

Aijaz H. Lone[1 ✉], Xuecui Zou[1], Debasis Das[2], Xuanyao Fong[2], Gianluca Setti[1] and Hossein Fariborzi[1]

Topologically protected spin textures, such as magnetic skyrmions, have shown the potential for high-density data storage and energy-efficient computing applications owing to their particle-like behavior, small size, and low driving current requirements. Evaluating the writing and reading of the skyrmion's magnetic and electrical characteristics is crucial to implementing these devices. In this paper, we present the magnetic heterostructure Hall bar device and study the anomalous Hall and topological Hall signals in these devices. Using different measurement techniques, we investigate the magnetic and electrical characteristics of the magnetic structure. We measure the skyrmion topological resistivity and the magnetic field at different temperatures. MFM imaging and micromagnetic simulations further explain the anomalous Hall and topological Hall resistivity characteristics at various magnetic fields and temperatures. The study is extended to propose a skyrmion-based synaptic device showing spin-orbit torque-controlled plasticity. The resistance states are read using the anomalous Hall measurement technique. The device integration in a neuromorphic circuit is simulated in a 3-layer feedforward artificial neural network ANN. Based on the proposed synapses, the neural network is trained and tested on the MNIST data set, where a recognition accuracy performance of about 90% is achieved. Considering the nanosecond reading/writing time scale and a good system level performance, these devices exhibit a substantial prospect for energy-efficient neuromorphic computing.

## INTRODUCTION

Magnetic skyrmions have been investigated for their applications in non-volatile data storage and computing applications[1–4]. These swirling spin structures have the advantage of being topologically protected against external perturbations[5–7]. Skyrmions are stabilized via the chiral Dzyaloshinskii–Moriya interaction (DMI) interactions in non-centrosymmetric magnetic compounds[8,9] and due to interface DMI originating in the thin film systems exhibiting broken inversion symmetry[10–12]. This chiral DMI antisymmetric exchange interaction responsible for forming magnetic skyrmions[13,14] emerges from the strong spin–orbit coupling at a heavy metal/ferromagnetic (HM/FM) interface with broken inversion symmetry[15–17]. The exchange coupling energy and anisotropy energy prefer spins' parallel and uniaxial alignment, but the DMI and dipolar energy terms prefer the noncollinear alignment of spins[18,19]. In asymmetric ferromagnetic multilayer systems, such as Pt/Co/Ta[20], Pt/CoFeB/MgO[12], and Ta/CoFeB/MgO[10], the DMI is obtained by the high interfacial spin–orbit coupling caused by symmetric breaking. Along with DMI, recent reports have shown that dipolar interactions can stabilize the skyrmions in a thin film system[21–23]. Also, some studies have demonstrated the existence of magnetic quasiparticles in nanomagnets without any DMI[24,25]. The authors showed that the geometry of a nanoparticle can also influence the skyrmion stability in such cases[26–28]. Skyrmionics as a sub-field of spintronics has gained substantial attention owing to the scalable and sub-nanometric skyrmion size of the skyrmions[29–31]. These properties of the skyrmions allow increased memory density[32]. Skyrmions can be stabilized at room temperature and driven by

current densities $\sim 1 \times 10^4$ A/cm[21,31], so writing into these devices is energy-efficient compared to its counterpart domain wall devices[33–36]. The intrinsic topological protection of the skyrmion gives it a lifetime and makes it stable against external perturbations[5,37]. Topological protection means that skyrmions have a characteristic topological integer that the continuous deformation of the field[38,39] can't change. Mathematically, the topological integer, also known as skyrmion charge or winding number, is given by

$$Q = \frac{1}{4\pi} \int \int \boldsymbol{m} \cdot \left( \frac{\partial \boldsymbol{m}}{\partial x} \times \frac{\partial \boldsymbol{m}}{\partial y} \right) dx dy \qquad (1)$$

The spins projected on the *xy*-plane and normalized magnetization vector $\boldsymbol{m}$ can be determined by the radial function $\theta$, Vorticity $Q_v$ and helicity $Q_h$:

$$m(r) = [\sin(\theta)\cos(Q_v\varphi + Q_h), \sin(\theta)\sin(Q_v\varphi + Q_h), \cos(\theta)]. \qquad (2)$$

The vorticity number is related to the skyrmion number as follows[4]:

$$Q = \frac{Q_v}{2}[\mathrm{Lim}_{r\to\infty}\cos(\theta(r)) - \cos(\theta(0))]. \qquad (3)$$

The skyrmions' topological characteristics or non-trivial geometry gives birth to an emergent electromagnetic field (EEMF)[40,41] that leads to other physical effects such as the topological Hall effect[42]. In a system with magnetic skyrmions, the conduction electrons move in a smoothly varying magnetic field. Thus, they adapt to the local magnetization of the skyrmion, and in the process, these electrons collect a quantum mechanical phase (Berry phase).

[1]Computer, Electrical and Mathematical Science and Engineering Division, King Abdullah University of Science and Technology (KAUST), Thuwal 23955-6900, Saudi Arabia. [2]Department of Electrical and Computer Engineering, National University of Singapore, Singapore 117583, Singapore. ✉email: aijaz.lone@kaust.edu.sa

Therefore, along with the normal Hall, which depends upon the external magnetic field and anomalous Hall effect, emerges out of magnetization[43,44]. The topological Hall effect is also expected to originate due to the skyrmions in these magnetic thin films. Thus, the reading of the skyrmions can be realized by evaluating the topological Hall effect in terms of extra contribution in the Hall signal. Recently, a few reports have shown the contribution of the skyrmion Hall resistivity in MnSi[8,45], [Pt/Co/Ir]$\times 10$[46], and 2D materials such as $Cr_2Te_3$ and $Cr_2Se_3$[47]. They are considering the scope and advancement of the Ta/CoFeB/MgO magnetic hetero-structures for their applications in spintronic devices[43–45,48] and especially skyrmionic devices[6,46–48]. It is imperative to evaluate and study these systems' magnetic and electrical characteristics. Furthermore, these systems have shown room-temperature skyrmions, and by studying these electrical characteristics, we indirectly capture their behavior in terms of topological resistivity.

Furthermore, the end of Moore's law, which drives the CMOS device scaling, is approaching. Among different beyond CMOS data storage and computing technological advancements, spintronic devices have shown a promising future[6,49]. Due to scalable size, topological protection, and minimal driving current requirements, skyrmion-based racetrack memories and computing technologies are being envisaged. Skyrmion-based neuromorphic computing has seen substantial interest in the research community[50,51]. Neuromorphic computing takes inspiration from the brain's highly complex but equally energy-efficient functioning. Skyrmion-based neuromorphic computing proposes devices that mimic the functioning of biological neurons and synapses. We can achieve energy-efficient and parallel unconventional computing power by using these artificial synapses as non-volatile conductors (weights) in a neural network and or by using the skyrmion-based neurons as computing units. However, few works on neuromorphic devices -based on skyrmion are available in the literature[52–54]. However, there is still a need for a clear understanding of the different reading mechanisms in these devices. This article presents a combination of experimental and micromagnetic studies to analyze anomalous Hall and topological Hall resistivity signatures in multilayer spintronic devices. These studies can advance the field of skyrmion-based data storage and computing and multilayer spintronic devices for neuromorphic computing in general. We present experimental and micromagnetic studies to evaluate the electrical and magnetic characteristics of the Ta/CoFeB/MgO thin film heterostructure system. Using the combination of different measurements like magnetometry at different temperatures, Hall measurement from 2 K to 300 K, and magnetic force microscopy imaging, we investigate these multilayers' magnetic and electrical characteristics. Using the measured total anomalous Hall resistivity and analytical models, we estimate the skyrmion topological resistivity at different temperatures as a function of the magnetic field. The anomalous and skyrmion topological resistivity studies in these heterostructures provide deeper insight into the realization of the spintronic devices for memory and logic. Such systems can use the anomalous Hall and topological resistivity as alternate reading mechanisms. Considering the complex interactions in a magnetic multilayer system, the tunnel magnetoresistance TMR reading of these systems is quite challenging. Thus, we can indirectly use the anomalous Hall and topological resistivity to probe the spintronic devices based on the multilayer systems. MFM imaging in different fields further supports the electrical characteristics presented in this manuscript. Motivated by the experimental results from anomalous and topological resistance and supported by the micromagnetic simulations, we propose a scaled version of the device as the Domain wall/ skyrmion synapse with high linearity. The anomalous Hall resistivity-based reading is utilized in the proposed synaptic device. Based on this multilayer synaptic device, the neural network shows 89.5% recognition accuracy on the MNIST data classification.
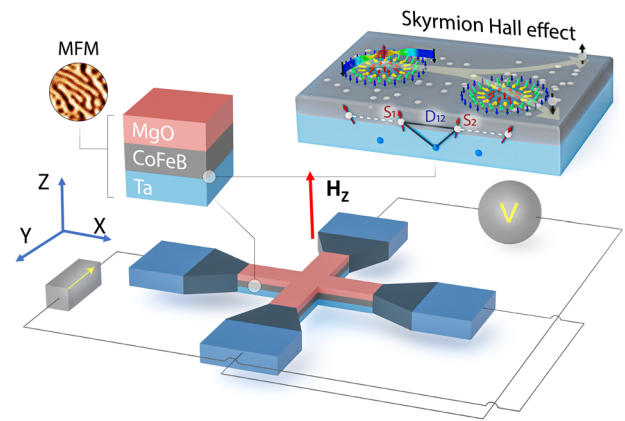


**Fig. 1 Magnetic multilayer device.** (Ta/CoFeB/MgO)$_{\times 15}$ multilayer device and the setup for Anomalous Hall measurements, Hz shows the direction of the external magnetic field.

## RESULTS AND DISCUSSION

The magnetic thin film system considered in this work is [Ta/CoFeB/MgO]$_{\times 15}$. The device for characterization and measurements is fabricated as a crossbar of size $50 \times 2.5$ μm$^2$, as shown in Fig. 1. The stack deposition and device fabrication details can be found in the supplementary material [Fig. S1a]. We considered 15 repetitions to stabilize small skyrmions at room temperature and zero fields for different CoFeB thicknesses. We observed skyrmions of around 300 ~ 400 nm in size. Sample exhibits admix of stripe domains, labyrinth domains, and skyrmions of size around 300 nm. The stack deposition quality was from the samples' cross-sectional transmission electron microscopy (TEM) and is shown in supplementary Fig. [S1b], where we observe Ta thickness around 5 nm, CoFeB thickness around 0.85 nm, and MgO 2 nm.

Figure 2a shows the magnetization-magnetic field (M-H) hysteresis loops measured using VSM for different samples with varying CoFeB thickness. The M-H loops show perpendicular magnetic anisotropy (PMA) in all the samples with thicknesses (of 0.5 nm to 1.1 nm). The butterfly shape characteristic of the multi-domain magnetic texture stabilization in the FM thin film is obtained in most samples. As observed, the multi-domain characteristics are shown for the CoFeB thickness ranging from 0.77 nm to 1.1 nm. The saturation magnetization increases linearly with increasing thickness, as shown in Fig. 2a. The switching field obtained from the VSM measurements is reduced for all the samples with more prevalent butterfly hysteresis, which indicates the magnetization switching by gradual multi-domain reversal. We observe that the CoFeB thickness ranging from 0.83 nm to 1.1 nm has a higher probability of stabilizing the skyrmions at room temperature. In Fig. 2b, the magnetic texture was obtained from MFM imaging for the sample with a thickness of 1 nm at zero field. The mixed phase with skyrmions of $Q = \pm 1$ and stripe domains is visible, as expected from the VSM measurements. To obtain the 3D view, the MFM picture view was tilted to observe the magnetic signal intensity as a z-component. Corresponding MFM images of the samples with varying CoFeB thickness in zero fields and at room temperature are shown in Fig. 2c–e. These samples' MFM probed magnetic texture reveals reducing stripe domain width with reducing CoFeB thickness from 0.95 nm down to 0.9 nm and 0.8 nm, which can be attributed to the increased surface anisotropy. For CoFeB thickness around 0.9 nm, most stripe domains collapse into skyrmion bubbles of diameter around 300 nm, as shown in Fig. 2c. The saturation magnetization ($M_s$) of the $t_F = 0.9$ nm is 0.73 emu/cm$^3$, which is greater than the $M_s$ for
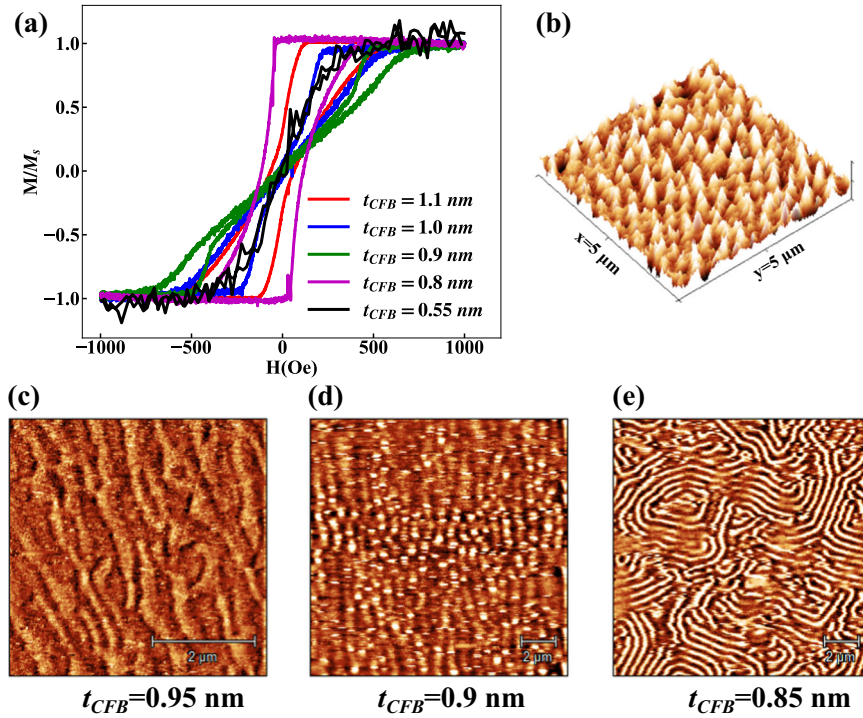
**Fig. 2 Magnetic characteristics dependence on film thickness. a** VSM magnetic hysteresis shows a butterfly shape (characteristics of multidomain/skyrmions) for magnetic layers' thickness (0.55 nm to 1.1 nm). **b** The tilted MFM picture of the sample with CoFeB thickness 0.95 nm shows room temperature fluctuations: The MFM picture view was tilted to observe the magnetic signal intensity as a *z*-component. MFM probed the magnetic texture of the samples at room temperature and zero fields for thickness (**c**) 0.95 nm, (**d**) 0.9 nm, and (**e**) 0.85 nm, showing different magnetic phases. The width of the stripe domains decreases on reducing thickness, indicating increased surface anisotropy. For CoFeB thickness around 0.9 nm, most stripe domains collapse into skyrmion bubbles of diameter around 400 nm. Note: The thicknesses are averaged over a 1 cm × 1 cm sample after dicing a wafer with wedge deposition (expected thickness (0.5 nm to 1.2 nm))

$t_F = 1$ nm, so in the case of 0.9 nm, the stray field is helping in skyrmion stability. We also observed non-hysteretic behavior for $t_F = 0.55$ nm due to the very low saturation magnetization for this case. The individual MH hysteresis loops are also provided in supplementary Fig. S2a.

### Anomalous hall resistance measurements

The sample hosting skyrmions in the sample with CoFeB thickness around 0.9 nm was patterned into $50 \times (2.5 \sim 3)$ μm$^2$ Hall bars, as shown in Fig. 3. The Hall measurements were carried out in the presence of a DC 500 μA and magnetic field.

Was swept in the range of ±10 KOe. Variations of anomalous Hall resistance ($R_{xy}$) with the applied magnetic field (H) are shown in Fig. 3a–c for various temperatures ranging from 2-300 K. The separate RH loops are also provided in supplementary Fig. S2b. For temperature T = 300 K, 250 K, and 200 K, we observe the butterfly loop behavior in $R_{xy}$ vs. H. These results are in line with the VSM-based MH loops as shown in Fig. 2. Figure 3c shows the anomalous Hall resistivity measured from (−200Oe to 600 Oe) to compare the slope of Rxy for the magnetic field for different temperatures. The butterfly-shaped resistance-magnetic field loops for T = 300 K, 250 K, and 200 K indicate the existence of the multidomain magnetization texture in the thin film. As shown in Fig. 3c, the slope of the resistance-field curve is the lowest at the temperature of 300 K, and the magnetization curve is quite linear. This behavior indicates the free layer magnetization switches through multidomain expansion/contraction at room temperature. The RH characteristics align with the MH characteristics observed in the VSM measurements, as shown in Fig. 2a. Furthermore, As the temperature is lowered, the anisotropy and saturation magnetization increase, so layers switch at higher fields.

At 200 K, although not completely vanished, we still observed some butterfly loop shape and analog switching behavior shifts from (200 Oe to 700 Oe) and (−200Oe to −700Oe). In magnetic materials, the Hall conductivity observed across transverse (x-y)-terminals contributes from the ordinary Hall effect due to the magnetic field, anomalous Hall effect due to the magnetization, and topological Hall effect of the skyrmions. The total Hall resistivity is given by the summation of the ordinary, topological, and anomalous resistivity and expressed mathematically as

$$\rho_{xy} = \rho^O + \rho^A + \rho^T = R_O B + R_S \mu_0 M_Z + R_O P B^z_{em} \quad (4)$$

where $R_O$ is the ordinary Hall coefficient, $B$ is the external magnetic field, $R_s$ is the anomalous Hall coefficient, $M_z$ is the magnetization component perpendicular to the film and $P$ is the spin polarization in the FM. The topological Hall resistance due to skyrmions emerges due to the emergent electromagnetic field seen by the conduction electrons. The conduction electrons couple with the local spin configuration of the skyrmion and acquire a Berry phase. The emergent magnetic field is given by[55]

$$B^e_Z = \frac{\Phi^e_z}{A} = -\frac{h}{eA} \iint \frac{1}{4\pi} \boldsymbol{m} \cdot \left(\frac{\partial \boldsymbol{m}}{\partial x} \times \frac{\partial \boldsymbol{m}}{\partial y}\right) dx dy \quad (5)$$

Which generates a topological resistivity:

$$\rho^T_{xy} = P R_o \left|\frac{h}{e}\right| \frac{1}{A} \quad (6)$$

Here, $P$ is the spin polarization of the conduction electrons, $Ro$ is the normal Hall coefficient, $h$ is the Planck's constant, e is the electron charge, A is the area of the cross-overlap, and $\frac{h}{e}$ is the flux quantum.
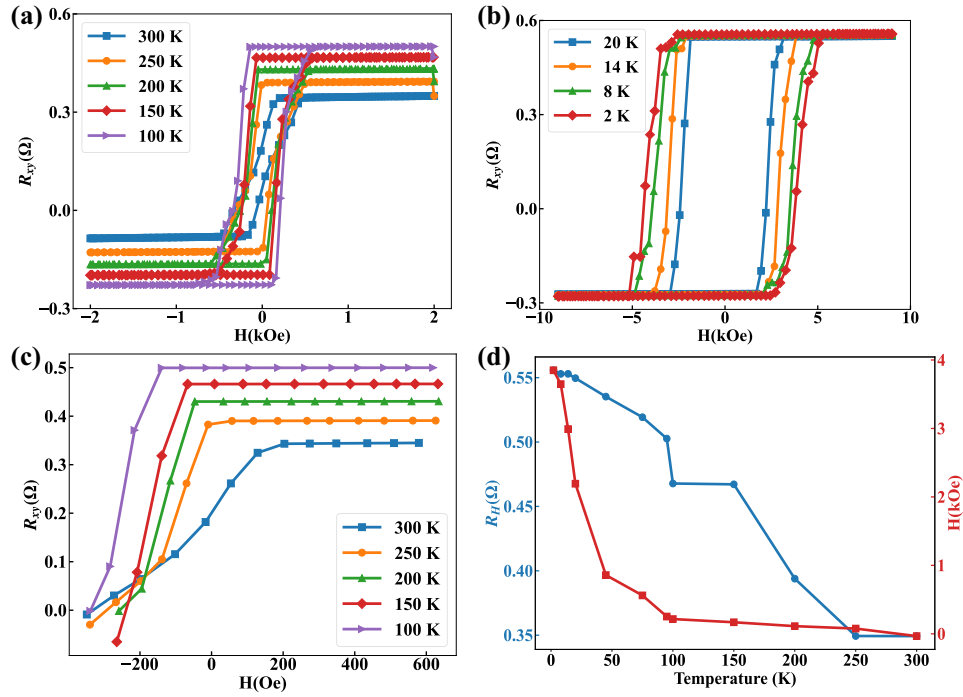
**Fig. 3 Electrical characteristics.** Anomalous Hall resistance of $R_{xy}$ with H for different temperatures (**a**)100-300 K, (**b**)2-20 K. **c** Anomalous Hall resistivity measured from ($-200$ Oe to 600 Oe) to compare the slope of Rxy for different temperatures. The free layer switches more linearly at room temperature (indicating DW changing across a more comprehensive field range). **d** Saturating Anomalous Hall resistance and switching field as a function of temperature.
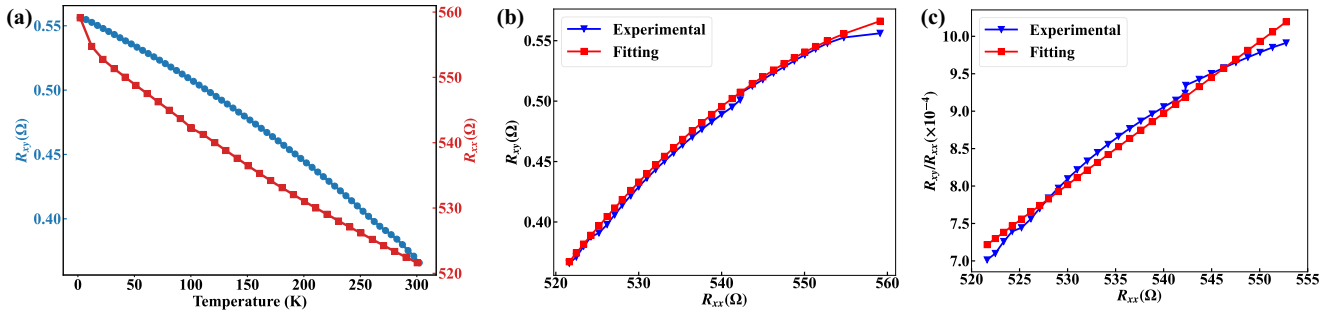


**Fig. 4 Transverse and longitudinal resistance. a** Anomalous Hall resistance and longitudinal resistance measured at temperatures 2 to 300 K, H = 1 T. **b** The Anomalous Hall resistance as a function of longitudinal resistance shows a quadratic behavior. **c** The $R_{xy}/R_{xx}$ vs $R_{xx}$ is fitted as a linear equation to obtain the (**a**, **b**).

To extract the topological resistivity from the measurement we first measured the normal Hall contribution as a linear fit to data at higher fields. The value of $R_O$ obtained is $1.44 \times 10^{-11}$ Ωm/T. The anomalous Hall effect completely dominates the Hall signal which is further proven by calculating the longitudinal conductivity $\sigma_{xx} \approx 0.5 \times 10^4$ (Ωcm$^{-1}$), implying that the device is behaving at the edge of bad metal region[49].

Figure 4a shows the temperature dependence of the anomalous Hall resistance and longitudinal resistance. We observe both resistances decreasing with increasing temperature which can be attributed to the weak localization or topological effects of skyrmions. In Fig. 4b we show the scaling of anomalous Hall resistivity concerning the longitudinal resistivity. The measured resistance values are taken at temperatures in the range of 2-300 K and magnetic field 1 T. $R_{xy}$ behaves as the second-order polynomial as shown by the analytical fitting of the measured resistance.

$$\rho_{XY} = a(\rho_{XX0} + \rho_{XX0}^2 + \rho_{XXT}^2) + b\rho_{XXT} \qquad (7)$$

where, $a = -8.78 \times 10^{-5}$, $b = 0.1002$, and $\rho_{xx0}$ is the longitudinal resistivity resistance at 2 K (approaching 0 K). The anomalous Hall resistivity in general is believed to have three main physical constituents, intrinsic scattering, skew scattering, and side jump. The skew scattering due to impurity and phonon shows a linear relation with $\rho_{xx}$ while intrinsic contribution with its origin in the berry-phase curvature and side jump due to spin-orbit interaction show a quadratic behavior.

In literature [40], the scaling of anomalous Hall resistivity with longitudinal resistivity in Fe magnetic thin films showed the significant contribution from intrinsic, side jump, and skew scattering. The skew scattering is predominantly dominated by residual resistivity with negligible contribution from phonon-induced resistivity. So, the proposed scaling is mathematically given by [40]:

$$\rho_{XY} = a\rho_{XX0} + \beta\rho_{XX0}^2 + b\rho_{XXT}^2 \qquad (8)$$

where $\alpha$ and $\beta$ are numerical constants.

Our measurements and analytical fitting reveal that the phonon contribution to the skew scattering term hence, anomalous Hall
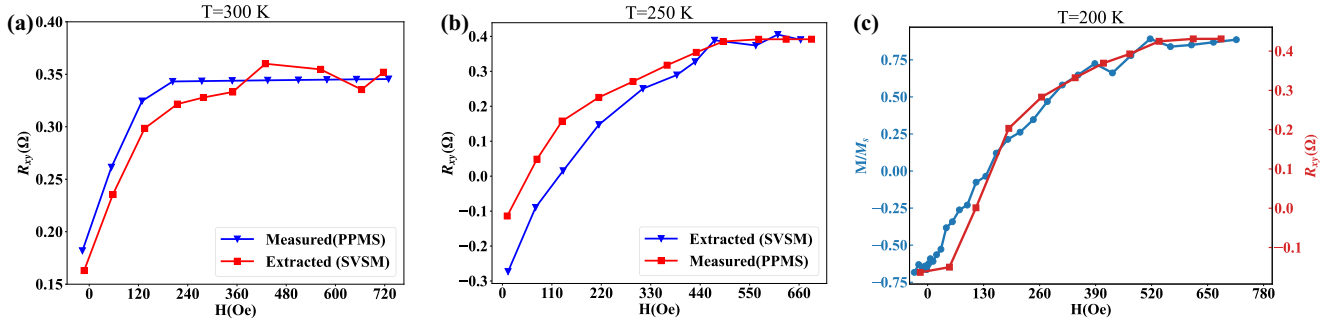
**Fig. 5 Relation between the electrical and magnetic characteristics. a** Anomalous Hall resistance and the normalized magnetization for T = 300 K. **b** Anomalous Hall resistance and extracted anomalous Hall resistance for T = 300 K. **c** Anomalous Hall resistance and extracted anomalous Hall resistance for T = 200 K.

resistivity is significant. To extract the value of constants $a$ and $b$ we divided $R_{xy}$ by the $R_{xx}$ and fit it to a linear equation given below.

$$\frac{\rho_{XY}}{\rho_{XX}} = a\rho_{XX} + c \tag{9}$$

The expected anomalous Hall resistivity depending only on the magnetization is given by

$$R_S M_Z \tag{10}$$

Where

$$R_S = a(\rho_{XX0} + \rho_{XX0}^2 + \rho_{XXT}^2) + b\rho_{XXT} \tag{11}$$

In squid VSM measurements researchers normally consider full magnetic thin film samples without any fabricated devices on the sample. In this study aiming for extracting the anomalous Hall resistance from the magnetization, we have considered 10 mm × 5 mm sample with on average 4 fabricated devices on it. The squid VSM performed on these samples with a few Hall bar devices is more accurate when compared to the measurements performed on the whole magnetic samples. The measurements were carried out at different temperatures from 300 K down to 2 K. Compared to the VSM measurements performed on the deposited samples, we observed the reduced saturation magnetization (by ~10²) due to reduced magnetic moments in the Hall bar. Also,

The magnetic saturation is more gradual as shown in Fig. 5a, c, indicating the switching by domain wall propagation and or skyrmion expansion/contraction. We expect the skyrmion topological resistivity to be more pronounced when measured devices are of small dimensions. Figure 5a, b shows the measured anomalous Hall resistance hysteresis and extracted anomalous resistance for temperatures T = 300 K and T = 250 K. The extracted anomalous Hall resistance follows the behavior of the measured magnetization and is shown in Fig. 5c shows the magnetization and anomalous Hall resistance at 200 K. The full anomalous Hall resistance hysteresis is provided in the supplementary material [Fig. S3]. In Fig. 5b, we observe a minor deviation between the resistance curves corresponding to the extracted anomalous Hall resistance and the measured anomalous Hall resistance. A similar difference between magnetization and resistance is noted in Fig. 5a, c. This minor deviation is attributed to the topological resistance due to skyrmion nucleation in the magnetic field range of 0 to 200 Oe.

The room temperature MFM images of the crossbar at 0 Oe, 50 Oe, 100 Oe, and 480 Oe are shown in Fig. 6. At 0 Oe, the observed skyrmion density is low, as seen in Fig. 6a, more skyrmion is nucleated as magnetic field increases as shown for 50 Oe in Fig. 6b. We observe the highest skyrmion density (normal and distorted) around 50 Oe to 100 Oe. A few stripe domains are kept in this field (see Fig. 6c). Finally, on increasing the magnetic

field to 480 Oe, the skyrmion density is reduced, and magnetization saturation is observed, but a few observed stripe domains remain. Note: The external magnetic field was applied via the lab-made electromagnet to reach $H_{max}$ = 490 Oe. The micromagnetic simulations at 0 K(2 K) shown in Fig. 8 show a similar magnetic texture evolution with the magnetic, as we observed in Fig. 6. (See supplementary video SV1).

We measured the topological resistivity for temperatures from 2 K to 300 K. Figure 7a–d shows the variations of topological resistivity due to skyrmions throughout the magnetic hysteresis for temperatures 300 K, 250 K, 200 K, and 50 K. In all cases, the topological resistivity is maximum in the low field regime, and it starts decreasing with the increasing field. For the temperature 300 K, the topological resistivity as a function of the magnetic field clearly shows a peak around 100 Oe, and resistivity decreases with increasing magnetic field, indicating skyrmion annihilation. Thus, topological resistivity follows the trend seen in MFM images, as shown in Fig. 6, and micromagnetic images, as shown in SV1. For the temperature, we observe at T = 50 K, the peak topological resistivity is 0.77 uΩcm, and resistivity decreases to 0.3 uΩcm for 300 K. Compared to 300 K at low temperatures, the possibility of stabilizing many skyrmions is high. This is due to increased DMI, anisotropy, and saturation magnetization. The DMI scaling with temperature is found to be much more robust than anisotropy and saturation magnetization. Furthermore, in Fig. 7e, f, we show the same topological resistivity after considering the anomalous Hall resistivity offset. In both cases for temperature T = 300 K and T = 200 K, we observe the decreasing topological Hall resistivity with the increasing field from 0 Oe 750 Oe. The only difference is visible for the negative magnetic field. If we don't consider the strange Hall offset correction, we observe a shift in the topological resistivity curve; even for higher negative magnetic fields, topological resistivity doesn't disappear (which we attribute to the shift in the anomalous Hall resistivity). But in comparison in Fig. 7e, f, we have adjusted the offset and recalculated the topological resistivity, which in this case approaches zero in both field directions. The topological resistivity for other temperatures is provided in supplementary Fig. S4.

In the presence of strong DMI and saturation magnetization $M_s$, the skyrmion density increases, and we observe that measured topological resistance is highest at the 2 K, as shown in Fig. 8b. The topological charge computed from micromagnetic simulations for a crossbar of dimensions (1024 × 256) nm2, at different temperatures, shows that at 0 K, the Q = −138; at 100 K, Q decreases to −127 for 200 K, the Q reduces to −66, and at 300 K the Q stabilizes to a value of −10. Note: The slight discrepancy between simulation and measured behavior is attributed to sample size differences and other interactions that can't be accommodated in the micromagnetic simulations. In large-size micrometric devices, the different magnetic effects such as
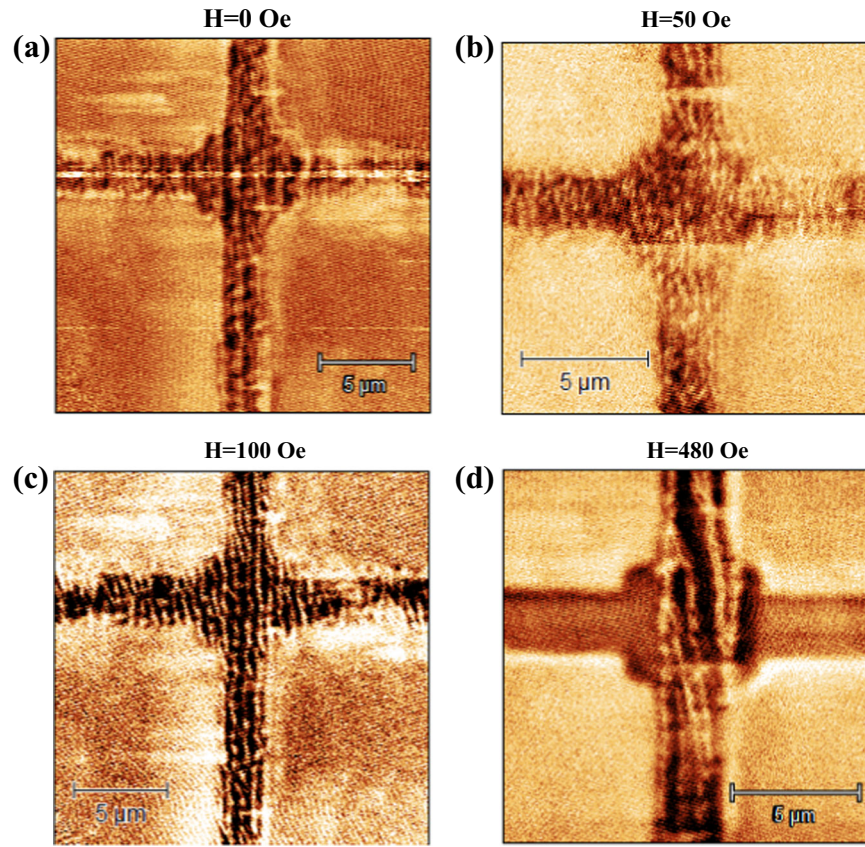
**Fig. 6  Room temperature MFM scans at different magnetic fields. a** H = 0 Oe (**b**) H = 50 Oe (**c**) H = 100 Oe (**d**) H = 480 Oe.

(anisotropic magnetoresistance AMR, planer Hall effect, skyrmion motion, etc.), electrical (measurement errors, leakage current via transverse arm), geometric (asymmetry in device design, thickness variations, etc.) and skyrmion-skyrmion, and skyrmion-edge effects or other quasi-particle interactions will be high. So, extracting the topological Hall resistivity with high accuracy is still challenging. Thus, we expect these minor discrepancies due to these effects. The decreasing skyrmion density/ topological charge at higher temperatures is shown in supplementary video SV2. To understand the relation between the topological resistivity and magnetic texture at 2 K, the micromagnetic simulations of the similar scaled crossbar device at 2 K are performed. As shown in Fig. 8b, the topological resistivity increases as the field is increased from 0 Oe to 3000 Oe, and we measured the peak value around 3000 Oe. Like in the case of all the temperature measurements, the topological resistivity starts decreasing with increasing field and becomes zero at 9000 Oe. The micromagnetic simulations at 2 K reveal that the topological charge increases with the field till 4200 Oe, and it remains constant till 8800 Oe, followed by an abrupt jump to zero. The topological charge, being an integer (±1), is independent of the skyrmion size.

This implies that the increasing magnetic field reduces the skyrmion size, which also changes the free layer magnetization. But the skyrmion density remains stable till the magnetic field 8800 Oe; this is reflected in the topological charge profile as shown in Fig. 8b. The topological resistivity due to skyrmions is given by

$$\rho_{xy}^T = PR_o \left| \frac{h}{e} \right| \frac{S}{A} \qquad (12)$$

where $S/A$ gives the skyrmion density as per Eq. (12) the topological resistivity should follow the topological charge

characteristics and remain stable at the peak value till 8800 Oe. But as the magnetic field is increased above 3000 Oe the topological resistivity decreases, as shown in Fig. 8a, b. In micromagnetic simulations, we observe that the skyrmion size reduces as the magnetic field increases, as shown in Fig. 8d. also see supplementary video [SV1]. To get the average size of the skyrmion, we focus on the evolution of one skyrmion and observe its evolution as the field is swept from (0 Oe to 9000 Oe). Using the Python code for MuMax post-processing, we extract the skyrmion size at different magnetic fields. Thus, by extracting the skyrmion size from the OVF files at increasing magnetic fields, we got an approximate skyrmion size evolution with growing field. We observe small skyrmions at 2 K, and the maximum skyrmion size obtained in the micromagnetic simulations is around 26 nm.

If we use the theoretical formalism provided by the[31,] the calculated range of skyrmion radius falls in the range (5 nm to 25 nm) depending upon A, K, and D. That, to a more significant extent matches with our micromagnetic simulations. We believe the nano track width substantially affects the skyrmion size and the stray field (As it depends upon the device dimensions). Also, the temperature is critical in the skyrmion's effective size. For 2 K the thermal fluctuations are almost negligible, so the effective size of the skyrmion is expected to be smaller compared to the room temperature case. A recent article[56] on the effect of skyrmion size on topological conductivity in which the momentum (k) - space description of the system is used for the small skyrmions reveals that the skyrmion topological conductivity should decrease monotonically with decreasing skyrmion size.

The topological Hall conductivity $\sigma_{xy}$ is given by the sum of the k-space Berry curvature $\Omega(\vec{k})$ over the occupied bands. So, with decreasing skyrmion size, the Brillouin zone BZ becomes significant, but the number of occupied bands is reduced. The
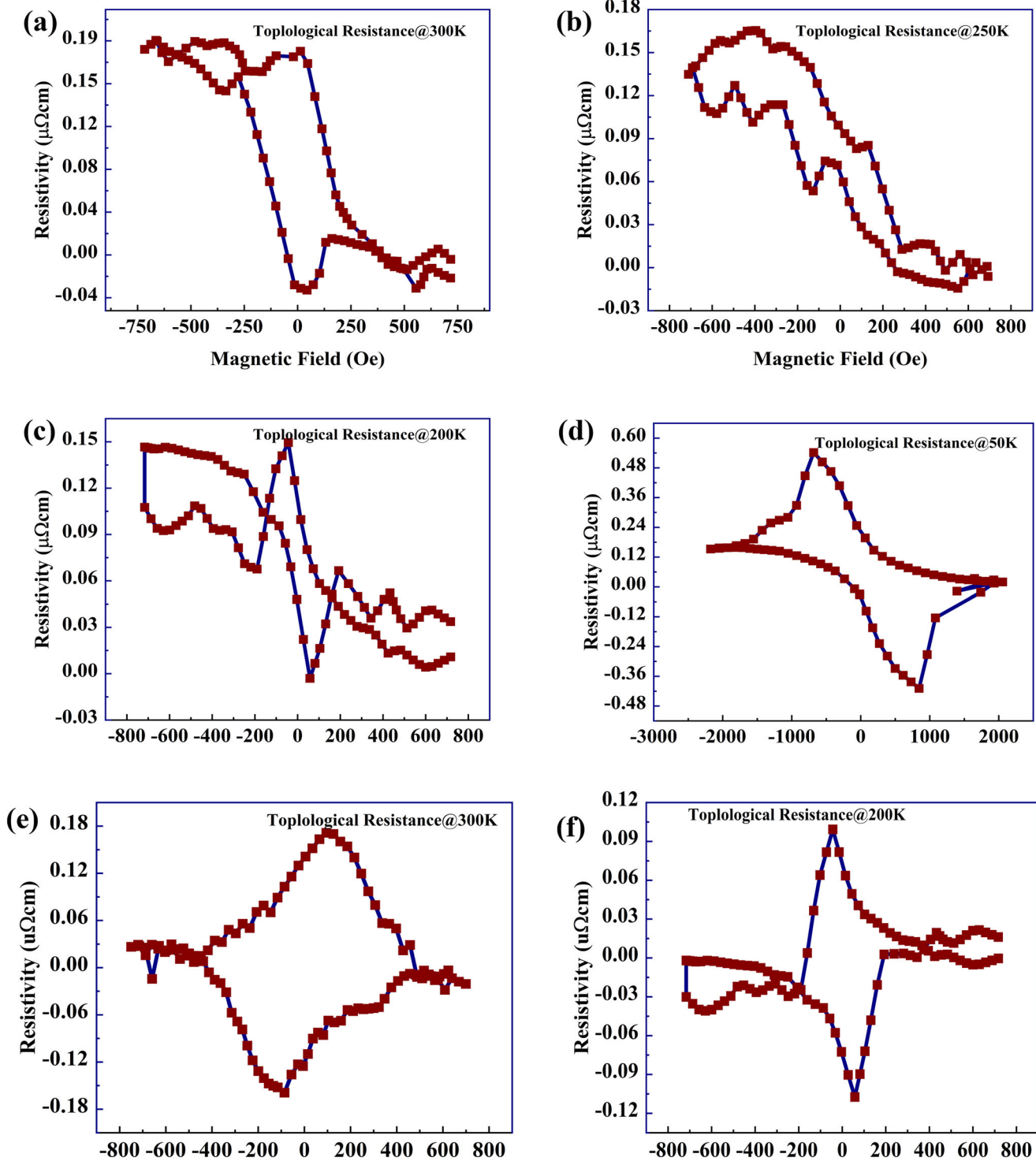
**Fig. 7 Topological resistivity.** Variation of Topological resistivity due to skyrmions throughout the magnetic hysteresis for temperatures (**a**) 300 K, (**b**) 250 K, (**c**) 200 K, (**d**) 50 K. **e** Topological resistivity after offset correction (in anomalous Hall resistivity) for the temperature (**e**) 300 K and (**f**) 200 K.

topological resistivity is given by the topological and longitudinal conductivity ratio (Eq. 13).

$$\rho_{xy} \cong -\frac{\sigma_{xy}}{\sigma_{xx}} \tag{13}$$

Thus, with decreasing skyrmion size, the topological resistivity also $\rho_{xy}$ also decreases, which is observed in Fig. 8a, b. Note: The

slight discrepancy between simulation and measured behavior is attributed to sample size differences and other interactions that can't be accommodated in the micromagnetic simulations. In large-size micrometric devices, the different magnetic effects such as (anisotropic magnetoresistance AMR, planer Hall effect, skyrmion motion, etc..), electrical (measurement errors, leakage current via transverse arm), geometric (asymmetry in device design, thickness variations, etc.) and skyrmion-skyrmion, and
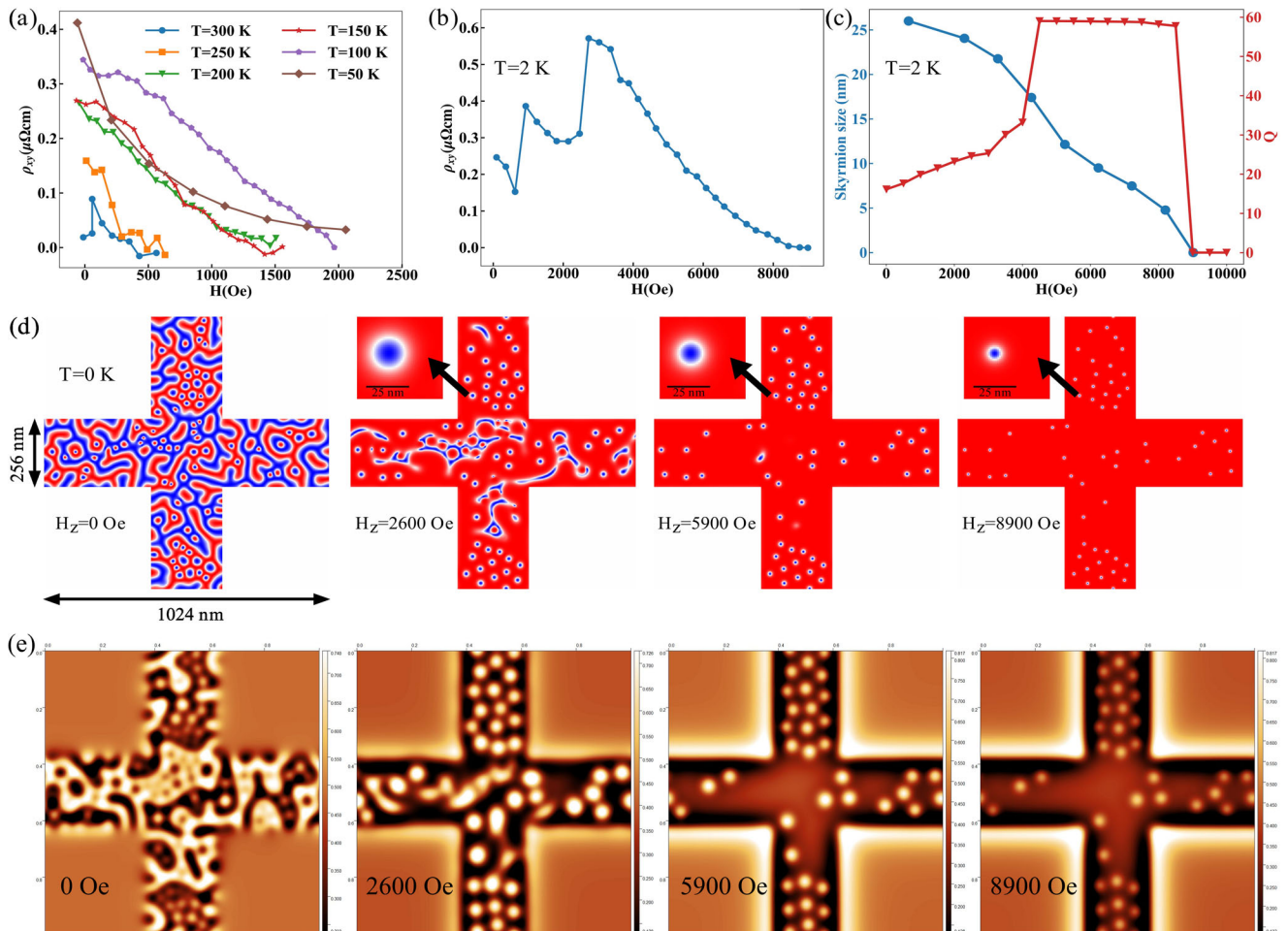
**Fig. 8 Topological resistivity explained with micromagnetics. a** Variation of $\rho_{xy}$ with the external magnetic field for temperatures T = 300 K, 250 K, 200 K, 150 K, 100 K, and 50 K (**b**) Variation of $\rho_{xy}$, (**c**) average skyrmion size and topological charge (Q) with the external magnetic field at T = 2 K. **d** Micromagnetic simulation results of the spin texture in a crossbar at the different magnetic field ($H_z$) performed at T = 2 K. **e** Micromagnetic MFM images of the corresponding magnetic textures shown in (**d**).

skyrmion-edge effects or other quasi-particle interactions will be high. So, extracting the topological Hall resistivity with high accuracy is still challenging. Thus, we expect these minor discrepancies due to these effects.

**Skyrmion-based synaptic device for neuromorphic computing**

To extend the applications of the anomalous Hall resistance and topological Hall resistance discussed presented in previous sections, In Fig. 9a, we propose the scaled version of the skyrmion-based Hall bar device for neuromorphic computing applications. The area of the ferromagnetic thin film (blue) considered in micromagnetic simulations is $1024 \times 128 \, nm^2$, while the thickness of the film is 0.9 nm. As shown in Fig. 9a, The proposed skyrmions-based synaptic device is divided into two regions: (1) a pre-synapse and (2) the (post-synapse) or active region.

The skyrmions/domains are driven into or out of the active region by passing a charge current from T-1 into T-2, generating the SOT. Depending upon the number of current pulses, the number of skyrmions/domains increases/decreases in the active region. This in turn changes the magnetization behavior of the active region. We compute the magnetization evolution from the MuMax and assign the corresponding resistance states from the measured devices. To read the resistance state of the device, we use the relation between measured anomalous Hall

resistance and the normalized magnetization (experiment), as shown in Fig. 9b. Then, we map the magnetization of the proposed device-free layer to the Hall resistance (measured experimentally), as shown in Fig. 9c. The characteristics of resistance potentiation and depression are shown in Fig. 9c. We observe a linear synaptic (non-linearity ≃ 0.05) behavior for both potentiation and depression. The device operation is visualized in the supplementary video [SV2]. The crossbar array of 4 devices shows the integration of the proposed device in the neuromorphic system. The input currents are applied between two terminals ($T_1$-$T_2$), and resistance is measured as anomalous Hall resistance across ($T_3$-$T_4$) terminals. ($I_1$- $I_2$) represent the input current and ($O_1$-$O_2$).

To address the device learning ability, we use the proposed synaptic devices as the neural network weights to train a 3-layer fully connected neural network FC-NN to classify the MNIST handwritten dataset (Fig. 9d). The network consists of three layers, including one input layer with 784 input neurons, a hidden layer with 100 neurons layer, and an output layer consisting of 10 neurons for 10-digit classification. The network is trained and tested on the MNIST dataset. We directly adopt the skyrmion-based synapse conductance and map these to the weights for network training. The stochastic gradient descent algorithm was used during the backpropagation step to train the network. Software-based perceptions in the same neural network architecture with ideal synaptic weights were used to benchmark this
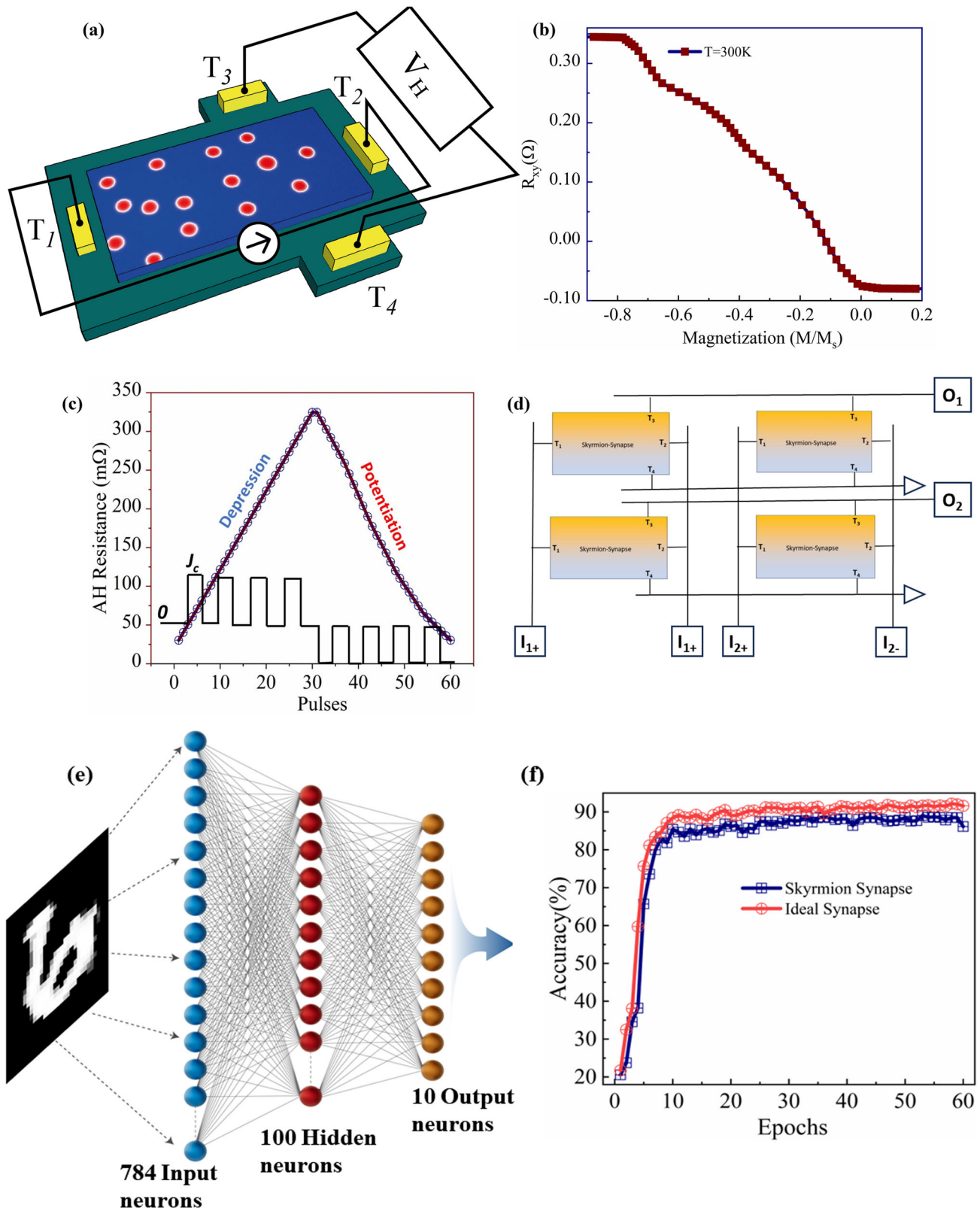
Fig. 9 Neuromorphic system simulations. a Synaptic device design $1024 \times 124$ nm$^2$ SOT writing and AHE reading. b Anomalous Hall resistance as a function of the normalized magnetization (c) synaptic potentiation and depression show highly linear behavior. d Crossbar circuit representation shows the proposed device's integration in the neuromorphic network. e 3-Layer fully connected neural network based on the proposed device. f Accuracy results achieved on MNIST data classification benchmarked with the ideal weights.

result. After the algorithm terminates, the accuracy of our synapse device achieves approximately 89.5%, which is slightly lower than the software default 91.5%, as shown in Fig. 9e. This highlights that, beyond low power, the skyrmion-based device provides a significantly good linearity and learning ability that appears well suited to the characteristics of edge learning tasks and neuromorphic computing hardware. Lastly, the proposed device structure and the reading mechanism apply to all types of magnetic textures (bubbles, vortices, domains, and skyrmions) driven by SOT or VCMA, which result in the change in the net magnetization of the magnetic system.

## CONCLUSION

In summary, we present the magnetic heterostructure Hall bar device and study the device's anomalous Hall and topological Hall signals. The proposed studies show a high resistance ON/OFF ratio devices where the abnormal Hall signals reading is utilized. The device has applications in Hall bar sensors and memory, especially for neuromorphic computing. The total anomalous Hall resistance is measured at 2 K to 300 K and correlated with the expected anomalous Hall resistance measured from Squid-VSM magnetization data. Memory devices at lower temperatures have applications in cryogenic electronics. Furthermore, the proper quantitative methodology will be followed, supported by MFM imaging and micromagnetic simulations. We show the topological Hall resistivity due to skyrmions at different temperatures and magnetic fields. Motivated by the possibility of using anomalous and topological resistivity as an alternate reading mechanism. We propose a scaled device version as the synapse and map the magnetization evolution with the measured anomalous Hall resistance. The device shows an excellent linear potentiation/depression with current pulses. When integrated into neural network architecture (simulated) for MNIST data classification, we observe an accuracy of up to 90%. Considering the nanosecond read/write pulse requirements in these synaptic devices. These studies and the proposed skyrmion device structure exhibit a better future for the energy-efficient and scalable neuromorphic spintronics.

## METHODS

### Fabrication and characterization

The stacks were deposited by magnetron sputtering onto 4-inch thermally oxidized Si wafers at room temperature. The bottom layer on the substrate is 300 nm silicon oxide by using thermal oxidization; then a multilayer stack is grown by using ultrahigh vacuum magnetron sputtering at room temperature in $5 \times 10^{-8}$ bar. The multilayer structure was, from the substrate side, A 300 nm SiO2 formed as an insulating layer, which is followed by growth of 10, 15, or 20 stacks of Ta (5 nm)/CoFeB(x)/MgO (2 nm), and finally formed a stack of $SiO_2(300 nm)/[Ta$ (5 nm)/CoFeB(x)/ MgO (2 nm)]$_{\times 15}$, where MgO layers were deposited by RF magnetron sputtering and the other layers were deposited by DC magnetron sputtering. The repeated deposition of Ta (5 nm)/ CoFeB(x)/MgO (2 nm) was designed to increase skyrmion thermal stability and decrease the skyrmion size. The thickness of CoFeB varies from 0.5 nm to 1.1 nm to find the optimum CoFeB thickness for stabilizing room-temperature skyrmions. Then, the deposited film was processed into micro-2.5 × 50 um² crossbars and followed by a lift-off process. To form electrical contacts. After the film deposition, we spin-coated AZ5214 photoresist of 1.6 um thickness with hardened bake for 2 mins at 110 °C to use it in a positive tone. Then, we patterned the crossbars on the resist using conventional photolithography. Ion beam etching using Ar gas removes the exposed magnetic stacks outside the resist mask. During the etching, we monitored the conductivity

of the etched region and stopped the etching when the signal from the 300-nm-thick silicon oxide layer appeared. To form electrical contacts, Ti (10 nm)/Au (100 nm) was deposited on the sides of the crossbars through sputtering at the rate of 0.8 nm/s. The electrical contact pads are defined using photolithography and lifting off by immersion in acetone with ultrasonic processing for 5 min. The magnetic characterization of the samples for thickness optimization was done using normal vibration sample magnetometry (VSM) at room temperature. Samples with CoFeB thickness ranging from (0.5 nm to 1.1 nm) were characterized. The deposition stack quality was confirmed with the cross-sectional TEM of the sample. After VSM, we performed the imaging of the samples with multi-domain magnetic characteristics using magnetic force microscopy (MFM) based on dimensional Icon SPM. For probing, we used CoIr coated MFM tip provided by Bruker Inc. The Hall measurements were done using a standard Hall measurement system Quantum Design PPMS capable of applying DC magnetic fields. We measured the crossbar devices at temperatures ranging from (2 K to 300 K) and at different magnetic fields depending upon the temperature. Furthermore, we performed the superconductor-vibration sample magnetometry (Squid-VSM) on a 4mmx8mm sample carrying four crossbar devices. Using the magnetization measured from Squid-VSM, we extracted the expected anomalous Hall resistivity. The MFM imaging of the devices in the presence of a magnetic field and the current was done to relate the magnetic texture to the magnetization and anomalous Hall resistivity.

### Micromagnetics

Magnetic skyrmions are described using their topological or skyrmion number Q, calculated using Eq. (1)[29].

The spins projected on the xy-plane and normalized magnetization vector $\boldsymbol{m}$ can be determined by the radial function $\theta$, Vorticity $Q_v$ and helicity $Q_h$ using Eq. (2).

The vorticity number is related to the skyrmion number using Eq. (3)[4]:

Micromagnetic simulations were performed using MuMax having the Landau–Lipschitz–Gilbert (LLG) equation as the basic magnetization dynamics computing unit[49]. The LLG equation describes the magnetization evolution as follows:

$$\frac{d\hat{\boldsymbol{m}}}{dt} = \frac{-\gamma}{1+a^2}[\boldsymbol{m} \times \boldsymbol{H_{eff}} + \boldsymbol{m} \times (\boldsymbol{m} \times \boldsymbol{H_{eff}})] \tag{14}$$

where $\boldsymbol{m}$ is the normalized magnetization vector, $\gamma$ is the gyromagnetic ratio, $a$ is the Gilbert damping coefficient, and

$$\boldsymbol{H_{eff}} = \frac{-1}{\mu_0 M_S} \frac{\delta E}{\delta \boldsymbol{m}} \tag{15}$$

is the effective MF around which the magnetization process occurs. The total magnetic energy of the free layer includes exchange, Zeeman, uniaxial anisotropy, demagnetization, and DMI energies[44,50].

$$E(\boldsymbol{m}) = \int_V [A_E(\nabla \boldsymbol{m})^2 - \mu_0 \boldsymbol{m}.H_{ext} - \frac{\mu_0}{2}\boldsymbol{m}.H_d - K_u(\hat{u}.\boldsymbol{m}) + \boldsymbol{\varepsilon_{DM}}]dv \tag{16}$$

where A is the exchange stiffness, $\mu_0$ is the permeability, Ku is the anisotropy energy density, $H_d$ is the demagnetization field, and $H_{ext}$ is the external field; moreover, the DMI energy density is then

**Table 1.** Micromagnetic simulation details.

| Grid Size | Cell Size (nm) | Anisotropy Ku (J/m$^3$) | Saturation Mag. Ms A/m | Exchange- Stiffness (AE) J/m | DMI J/m$^2$ |
|---|---|---|---|---|---|
| 1024, 1024, 1 | 1, 1, 0.83 | $1 \times 10^6$ | $1 \times 10^6$ | $1 \times 10^{-11}$ | $3.0 \times 10^{-12}$ |

computed as follows:

$$\varepsilon_{DM} = D[m_z(\nabla . \boldsymbol{m}) - (\boldsymbol{m}.\nabla).\boldsymbol{m}] \tag{17}$$

The spin–orbit torque is then added in the form of modified STT in MuMax[57].

$$\boldsymbol{\tau}_{SOT} = -\frac{\gamma}{1+\alpha^2} a_J[(1+\xi\alpha)\boldsymbol{m}\times(\boldsymbol{m}\times\boldsymbol{p}) + (\xi-\alpha)(\boldsymbol{m}\times\boldsymbol{p})] \tag{18}$$

$$a_J = \left|\frac{\hbar}{2M_S e\mu_0}\frac{\theta_{SH} j}{d}\right| \text{ and } \boldsymbol{p} = sign(\theta_{SH})\boldsymbol{j}\times\boldsymbol{n}$$

where $\theta_{SH}$ is the spin Hall coefficient of the material, $j$ is the current density, and $d$ is the free layer thickness.

The micromagnetic simulation details are given in the Table 1.

## DATA AVAILABILITY

The data supporting this study and its findings are available within the article, its Supplementary Information, and associated files (response files). The codes can be provided by the authors on a reasonable request.

## REFERENCES

1. Fert, A., Reyren, N. & Cros, V. Magnetic skyrmions: Advances in physics and potential applications. *Nat. Rev. Mater.* **2**, 17031 (2017).
2. Finocchio, G., Büttner, F., Tomasello, R., Carpentieri, M. & Kläui, M. Magnetic skyrmions: From fundamental to applications. *J. Phys. D. Appl. Phys.* **49**, 423001 (2016).
3. *Magnetic Skyrmions and Their Applications. Magnetic Skyrmions and Their Applications.* https://doi.org/10.1016/c2019-0-02206-6 (2021).
4. Kang, W., Huang, Y., Zhang, X., Zhou, Y. & Zhao, W. Skyrmion-electronics: an overview and outlook. *Proceedings of the IEEE* **104**, 2040–2061 (2016).
5. Bazeia, D., Ramos, J. G. G. S. & Rodrigues, E. I. B. Topological strength of magnetic skyrmions. *J Magn Magn Mater* **423**, 411–420 (2017).
6. Yang, S. H., Naaman, R., Paltiel, Y. & Parkin, S. S. P. Chiral spintronics. *Nat. Rev. Phys.* **3**, 328–343 (2021).
7. Bergmann, G. The anomalous hall effect. *Phys. Today* **32**, 25–30 (1979).
8. Neubauer, A. et al. Topological hall effect in the a phase of MnSi. *Phys. Rev. Lett.* **102**, 1–4 (2009).
9. Li, Y. et al. Robust formation of skyrmions and topological hall effect anomaly in epitaxial thin films of MnSi. *Phys. Rev. Lett.* **110**, 1–5 (2013).
10. Qin, Z. et al. Stabilization and reversal of skyrmion lattice in Ta/CoFeB/MgO multilayers. *ACS Appl. Mater. Interfaces* **10**, 36556–36563 (2018).
11. Zhou, Y., Mansell, R. & van Dijken, S. Voltage control of skyrmions: Creation, destruction, and zero-magnetic field stabilization. *Appl. Phys. Lett.* **118**, 172409 (2021).
12. Woo, S. et al. revealed by time-resolved X-ray microscopy. *Nat. Commun.* **8**, 1–8 (2017).
13. Rohart, S. & Thiaville, A. Skyrmion confinement in ultrathin film nanostructures in the presence of Dzyaloshinskii-Moriya interaction. *Phys. Rev. B Condens Matter Mater Phys* **88**, 1–8 (2013).
14. Bernand-Mantel, A., Muratov, C. B. & Simon, T. M. Unraveling the role of dipolar versus Dzyaloshinskii-Moriya interactions in stabilizing compact magnetic skyrmions. *Phys Rev B* **101**, 45416 (2020).
15. Dijk, B. Van. Skyrmions and the Dzyaloshinskii-Moriya Interaction. *Thesis* 75 https://studenttheses.uu.nl/handle/20.500.12932/19275 (2014).
16. Mulkers, J., Van Waeyenberge, B. & Milošević, M. V. Effects of spatially engineered Dzyaloshinskii-Moriya interaction in ferromagnetic films. *Phys. Rev. B* **95**, 1–8 (2017).
17. Jadaun, P. The microscopic origin of DMI in magnetic bilayers and prediction of giant DMI in new bilayers. *NPJ Comput Mater.* https://doi.org/10.1038/s41524-020-00351-1 (2020).
18. Woo, S. et al. Deterministic creation and deletion of a single magnetic skyrmion observed by direct time-resolved X-ray microscopy. *Nat Electron* **1**, 288–296 (2018).
19. Bhattacharya, D. et al. Creation and annihilation of non-volatile fixed magnetic skyrmions using voltage control of magnetic anisotropy. *Nat Electron* **3**, 539–545 (2020).
20. Woo, S. et al. Observation of room-temperature magnetic skyrmions and their current-driven dynamics in ultrathin metallic ferromagnets. *Nat. Mater.* **15**, 501–506 (2016).
21. Ezawa, M. Giant Skyrmions stabilized by dipole-dipole interactions in thin ferromagnetic films. *Phys. Rev. Lett.* **105**, 1–4 (2010).
22. Utesov, O. I. Thermodynamically stable skyrmion lattice in a tetragonal frustrated antiferromagnet with dipolar interaction. *Phys. Rev. B* **103**, 1–10 (2021).
23. Montoya, S. A. et al. Tailoring magnetic energies to form dipole skyrmions and skyrmion lattices. *Phys. Rev. B* **95**, 1–10 (2017).
24. Kravchuk, V. P. et al. Topologically stable magnetization states on a spherical shell: Curvature-stabilized skyrmions. *Phys. Rev. B* **94**, 144402 (2016).
25. Yang, J., Abert, C., Suess, D. & Kim, S. K. Intrinsic DMI-free skyrmion formation and robust dynamic behaviors in magnetic hemispherical shells. *Sci Rep.* **11**, 3886 (2021).
26. Tejo, F. et al. Stabilization of magnetic skyrmions on arrays of self-assembled hexagonal nanodomes for magnetic recording applications. *ACS Appl. Mater. Interfaces* **12**, 53454–53461 (2020).
27. Carvalho-Santos, V. L., Corona, R. M., Altbir, D. & Castillo-Sepúlveda, S. Shifts in the skyrmion stabilization due to curvature effects in dome- And antidome-shaped surfaces. *Phys. Rev. B* **102**, 024444 (2020).
28. Kravchuk, V. P. et al. Multiplet of skyrmion states on a curvilinear defect: reconfigurable skyrmion lattices. *Phys. Rev. Lett.* **120**, 067201 (2018).
29. Everschor-Sitte, K., Masell, J., Reeve, R. M. & Kläui, M. Perspective: Magnetic skyrmions - Overview of recent progress in an active research field. *J. Appl. Phys.* **124**, 240901 (2018).
30. Yang, J. C., Mao, Q. Q. & Shi, Y. Shape of a skyrmion. *J. Phys. Condensed Matter* **31**, 165802 (2019).
31. Wang, X. S., Yuan, H. Y. & Wang, X. R. A theory on skyrmion size. *Commun. Phys.* **1**, 1–7 (2018).
32. Back, C. et al. The 2020 skyrmionics roadmap. (2020).
33. Tomasello, R. et al. A strategy for the design of skyrmion racetrack memories. *Sci. Rep.* **4**, 1–18 (2014).
34. Schellekens, A. J., Van Den Brink, A., Franken, J. H., Swagten, H. J. M. & Koopmans, B. Electric-field control of domain wall motion in perpendicularly magnetized materials. *Nat. Commun.* **3**, 847 (2012).
35. Kang, W. et al. A comparative study on racetrack memories: domain wall vs. skyrmion. *Proceedings - 7th IEEE Non-Volatile Memory Systems and Applications Symposium, NVMSA 2018* **1**, 7–12 (2018).
36. Fillion, C. E. et al. Gate-controlled skyrmion and domain wall chirality. *Nat. Commun.* **13**, 5257 (2022).
37. Wild, J. et al. Entropy-limited topological protection of skyrmions. *Sci. Adv.* **3**, 1–11 (2017).
38. Yin, G. et al. Topological charge analysis of ultrafast single skyrmion creation. *Phys. Rev. B* **93**, 1–7 (2016).
39. Je, S. G. et al. Direct demonstration of topological stability of magnetic skyrmions via topology manipulation. *ACS Nano* **14**, 3251–3258 (2020).
40. Nagaosa, N. & Tokura, Y. Topological properties and dynamics of magnetic skyrmions. *Nat. Nanotechnol.* **8**, 899–911 (2013).
41. Schulz, T. et al. Emergent electrodynamics of skyrmions in a chiral magnet. *Nat. Phys.* **8**, 301–304 (2012).
42. Bruno, P., Dugaev, V. K. & Taillefumier, M. Topological Hall effect and Berry phase in magnetic napostructures. *Phys. Rev. Lett.* **93**, 1–4 (2004).
43. Nagaosa, N., Sinova, J., Onoda, S., MacDonald, A. H. & Ong, N. P. Anomalous Hall effect. *Rev .Mod. Phys.* **82**, 1539–1592 (2010).
44. Seki, S. & Mochizuki, M. *Skyrmions and Electric Fields by Electric Fields.* (2016).
45. Karplus, R. & Luttinger, J. M. Hall effect in ferromagnetics. *Phys. Rev.* **95**, 1154–1160 (1954).
46. Zeissler, K. et al. Discrete Hall resistivity contribution from Néel skyrmions in multilayer nanodiscs. *Nat. Nanotechnol.* **13**, 1161–1166 (2018).
47. Jeon, J. H. et al. Emergent topological hall effect from exchange coupling in ferromagnetic Cr2Te3/Noncoplanar Antiferromagnetic Cr2Se3Bilayers. *ACS Nano* **16**, 8974–8982 (2022).

48. Li, S. et al. Experimental demonstration of skyrmionic magnetic tunnel junction at room temperature. *Sci Bull (Beijing)* **67**, 691–699 (2022).

49. Dieny, B. et al. Opportunities and challenges for spintronics in the microelectronics industry. *Nat. Electron.* **3**, 446–459 (2020).

50. Phys, J. A. & Kent, A. D. Skyrmionics — Computing and memory technologies based on topological excitations in magnets Skyrmionics — Computing and memory technologies based on topological excitations in magnets. **070908**, (2021).

51. Lone, A. H. & Fariborzi, H. Skyrmion-magnetic tunnel junction synapse with long-term and short-term plasticity for neuromorphic computing. *IEEE Trans Electron Devices* **70**, 371–378 (2022).

52. Chen, X. et al. A compact skyrmionic leaky-integrate-fire spiking neuron device. *Nanoscale* **10**, 6139–6146 (2018).

53. Huang, Y., Kang, W., Zhang, X., Zhou, Y. & Zhao, W. Magnetic skyrmion-based synaptic devices. *Nanotechnology* **28**, 08LT02 (2017).

54. Song, K. M. et al. Skyrmion-based artificial synapses for neuromorphic computing. *Nat Electron* **3**, 148–155 (2020).

55. Aharonov, Y., Stern Raymond, A., Sackler, B. & Berry, by. *Origin of the Geometric Forces Accompanying Berry's Geometric Potentials The investigation of the geometric phase [ll, initiated.* **69** (1992).

56. Matsui, A., Nomoto, T. & Arita, R. Skyrmion-size dependence of the topological Hall effect: a real-space calculation. *Phys. Rev. B* **104**, 1–6 (2021).

57. Vansteenkiste, A. et al. The design and verification of MuMax3. *AIP Adv.* **4**, 0–22 (2014).

## ACKNOWLEDGEMENTS

## AUTHOR CONTRIBUTIONS

A.H. Lone conceived the idea and fabricated the devices along with X.Zou. A.H. Lone did the characterization of the devices, performed the micromagnetic simulations, and analyzed the results. The paper was written by A.H. Lone with support from D.Das, K.Fong, G.Setti and H.Fariborzi. The project was supervised by H.Fariborzi and G.Setti.

## COMPETING INTERESTS

The authors declare no competing interests.

## ADDITIONAL INFORMATION

**Supplementary information** The online version contains supplementary material available at https://doi.org/10.1038/s44306-023-00006-z.

**Correspondence** and requests for materials should be addressed to Aijaz H. Lone.

**Reprints and permission information** is available at http://www.nature.com/reprints

**Publisher's note** Springer Nature remains neutral with regard to jurisdictional claims in published maps and institutional affiliations.